

# Micro-mesoporous carbons from cyclodextrin nanosponges enabling high capacity silicon anodes and sulfur cathodes for lithiated Si-S batteries

Mojtaba Alidoost<sup>[a]</sup>, Anna Mangini<sup>[a]</sup>, Fabrizio Caldera<sup>[b]</sup>, Anastasia Anceschi<sup>[c]</sup>, Julia Amici<sup>[a] \*</sup>, Daniele Versaci<sup>[a]</sup>, Lucia Fagiolarì<sup>[a]</sup>, Francesco Trotta<sup>[b]</sup>, Carlotta Francia<sup>[a]</sup>, Federico Bella<sup>[a]</sup>, and Silvia Bodoardo<sup>[a]</sup>

**Abstract:** Manufactured globally on industrial scale, cyclodextrins (CD) are cyclic oligosaccharides produced by enzymatic conversion of starch. Their typical structure of truncated cone can host a wide variety of guest molecules to create inclusion complexes; indeed, we daily use CD as unseen components of food, cosmetics, textiles and pharmaceutical excipients. The synthesis of active material composites from CD resources can enable or enlarge the effective utilization of these products in the battery industry with some economical as well as environmental benefits. New and simple strategies are here presented for the synthesis of nanostructured silicon and sulfur composite materials with carbonized hyper cross-linked CD (nanosponges) that show satisfactory performance as high capacity electrodes. For the sulfur cathode, the mesoporous carbon host limits polysulfide dissolution and shuttle effects and guarantees stable cycling performance. The embedding of silicon nanoparticles into the carbonized nanosponge allows to achieve high capacity and excellent cycling performance. Moreover, due to the high surface area of the silicon composite, the characteristics at the electrode/electrolyte interface dominate the overall electrochemical reversibility, opening a detailed analysis on the behavior of the material in different electrolytes. We show that the use of commercial LP30 electrolyte causes a larger capacity fade and this is associated with different solid electrolyte interface layer formation and it is also demonstrated that fluoroethylene carbonate addition can significantly increase the capacity retention and the overall performance of our nanostructured Si/C composite in both ether-based and LP30 electrolytes. As a result, an integration of the Si/C and S/C composites is proposed to achieve a complete lithiated Si-S cell.

## Introduction

Lithium-ion batteries enjoyed widespread adoption in many applications for energy storage due to their high rate capability, long calendar life and mostly for the high specific energy.<sup>[1]</sup> To date, driving researches on nanostructured active materials and advanced chemistries<sup>[2,3]</sup> gave new lease of life to the present Li-ion technology; however, there is still much room for increasing the battery energy density, pushing towards materials that could either display greater redox potentials or larger capacities than commercially available ones.<sup>[4,5]</sup>

Among the anodes, silicon-based ones show superior theoretic specific capacities (i.e., theoretic specific capacities of 3579 mAh g<sup>-1</sup> for Li<sub>15</sub>Si<sub>4</sub> and 4200 mAh g<sup>-1</sup> for Li<sub>22</sub>Si<sub>5</sub> alloys).<sup>[6,7]</sup> On the other hand, based on the conversion reaction between lithium and sulphur,<sup>[8]</sup> the sulphur cathode stands out as promising, mainly for its extraordinarily high theoretical specific capacity (1672 mAh g<sup>-1</sup>).<sup>[9]</sup> This could translate into ~500 Wh kg<sup>-1</sup> practical gravimetric energy density for the sulphur battery,<sup>[10]</sup> in comparison to the practical gravimetric energy<sup>[11]</sup> of ~240 Wh kg<sup>-1</sup> of current Li-ion technology.<sup>[12]</sup> There are multiple advantages of using sulfur and silicon as active materials for the cathode and anode, respectively. Both are inexpensive, highly available, nontoxic and characterized by high gravimetric capacities, as above mentioned. However, both sulfur and silicon come along with their own drawbacks.

The major issue addressed to crystalline silicon is its transformation into amorphous alloy with lithium, accompanied by a huge volumetric change<sup>[13]</sup> and some residual alloy phase, which remains unconverted after the first delithiation. During battery cycling, pulverization of the active material along with disconnection between the active material and the current collector result in rapid capacity fading and limited cycle life.<sup>[14]</sup> Such volumetric expansion/contraction of silicon causes solid electrolyte interface (SEI) disruption, which exposes new fresh surface to the electrolyte with consequent SEI thickening and electrolyte depletion.<sup>[15,16]</sup> Notably, to tackle these issues a systematic control of the material size to nanometer scale and the establishment of porous structures that relieve stresses and strains have been addressed.<sup>[17,18]</sup> The development of Si/C composites with different carbonaceous materials like graphite,<sup>[19]</sup> graphene,<sup>[20]</sup> porous carbons<sup>[21]</sup> and carbon nanotubes<sup>[7]</sup> has expanded the possibilities to achieve hierarchical structures that provide elastic behaviour, thus buffering for volume modifications. In this way, protective carbon shells assured the integrity of both silicon and SEI films.

Similarly, sulfur cathodes encountered problems of low sulfur utilization, low Coulombic efficiency, fast capacity fading and narrow cycle life.<sup>[22]</sup> These drawbacks arise mainly from polysulfide dissolution, which results in active-material loss at the cathode, Li-metal corrosion at the anode and insulating Li<sub>2</sub>S deposition on electrode surface during cell cycling and resting.

- [a] Dr. M. Alidoost, A. Mangini, Dr. J. Amici, Dr. D. Versaci, Dr. L. Fagiolarì, Prof. C. Francia, Prof. F. Bella, Prof. S. Bodoardo  
Department of Applied Science and Technology (DISAT),  
Politecnico di Torino, C.so Duca degli Abruzzi 24, 10129 Torino,  
Italy
- [b] Dr. F. Caldera, Prof. F. Trotta  
<sup>b</sup>Department of Chemistry, Università degli Studi di Torino, Via  
Pietro Giuria 7, 10125 Torino, Italy.
- [c] Dr. A. Anceschi  
CNR-STIIMA, Istituto di Sistemi e Tecnologie Industriali Intelligenti  
per il Manifatturiero Avanzato, Consiglio Nazionale delle Ricerche,  
C.so Pella 16, 13900 Biella, Italy.

[a]\* Corresponding author. Tel.: +39 (0)110904638; E-mail:  
julia.amici@polito.it  
Supporting information for this article is given via a link at the end of  
the document.

## FULL PAPER

Similarly, low conductivity of sulfur ( $5 \times 10^{-30} \text{ S}\cdot\text{cm}^{-1}$ ) [23] and volumetric expansions of  $\sim 80\%$  are reported, which are related to differences in the density between sulfur ( $2.07 \text{ g cm}^{-3}$ ) and  $\text{Li}_2\text{S}$  ( $1.66 \text{ g cm}^{-3}$ ). [8] To successfully operate, sulfur must be well combined with lightweight conductive additives and these are again carbons, usually with large surface area and suitable porosity to achieve fast kinetics. [24,25]

Rational design of hollow structures [26] and flexible carbon supports [27] allowed to load adequate amounts of elemental sulfur and buffer the volume expansions during cycling. Indeed, for the huge demand of energy storage devices, the production of high-quality carbons through cheap and sustainable means has also become a necessity. In this respect, cyclodextrins are bio-materials that find various applications in the form of bio-polymers [28] and, recently, their use has also been extended to batteries and supercapacitors. [29–32] Most of all,  $\beta$ -cyclodextrins (CD) are suitable building blocks for polymer syntheses since the cross-linking of CD with a variety of chemicals (including dianhydrides, diisocyanates, active carbonyl compounds, epoxides, carboxylic acids) produces insoluble highly cross-linked 3D network polymers known as nanosponges (NS), [33] for which their dimension and stiffness are dependent on the amount and type of crosslinker used. [34] The synthesis of these 3D bio-polymers (CDNS) opens up new avenues to obtain porous carbons that can be used as scaffolds for the preparation of composite materials for batteries, [35] leading to biochar yields ( $> 40\%$  at  $800^\circ\text{C}$ ) higher than most of biomass products, including grass, sawdust, peanut shell, shrimp hull, etc. [36]

Due to the tuneable synthesis, this class of polymers is a suitable precursor to produce activated carbon microfibers [37] and carbons with different porosity. [38]

Herein, carbonized nanosponges (CNS) from CDNS are used for the fabrication of nanostructured silicon and sulfur composites with excellent performance. Inspired from template methods, in which bimodal mesoporous carbons are obtained by tailoring the ratio between methylated CD and tetramethyl orthosilicate, [39] we used fumed silica powder as template agent to obtain hierarchical meso-porous carbons from carbonization of 3D NS. Because of their abundant and adjustable pore structure, the CNS can load an appropriate amount of active sulfur and also buffer the volume changes of sulfur active material during discharge and charge. We also investigate in detail and for the first time the extraordinary versatility of NS for the preparation of high-capacity nanostructured Si/CNS composites (Si@CNS), using CNS as a “backbone” structure to anchor silicon nanoparticles (Si NPs). We exploited the simplicity of introducing Si NPs during the cross-linking of CD in order to achieve a perfect embedding of silicon inside the 3D polymer structure before carbonization. Once the Si@CNS composite is obtained, further wrapping with reduced graphene oxide (rGO) results in a structured material (Si@CNS-rGO) that supplements good conductivity and flexibility [15,16] and assures long and stable cycling performances at relatively high current regimes (1C). In principle, the lithiated Si@CNS-rGO can be suitable to replace the lithium metal anode in the sulfur cell.

Such investigation is of huge interest since the use of lithium leads to dendrite formation and safety issues, reductive corrosion of lithium as a result of self-reduction of soluble polysulfides (shuttling), depletion of electrolyte limiting the cycle life, etc. For these reasons, lithiated silicon–sulfur batteries exploiting the benefits of quasi-solid electrolytes, [40] structured hosts for both

silicon and sulfur, [41,42] and high areal capacity electrodes [43] have been successfully developed. Motivated by this goal, we have focused our attention on the electrolyte formulation for testing the anode, trying to understand the compatibility of Si@CNS-rGO with the electrolytes of the sulphur cell. We deeply investigated the interfacial characteristics of Si@CNS-rGO composites in ether-based electrolytes, because the electrochemical performance of nanostructured silicon significantly depends not only on the electrolyte, but also on the structure of the material employed. This is the consequence of the characteristics of the SEI, which is related to both the surface properties of the active material and to the electrolyte composition. We have observed better capacity retention for Si@CNS-rGO in ether-based electrolytes in which fluoroethylene carbonate (FEC) additive replaced the traditional  $\text{LiNO}_3$  used to protect the lithium anode in the Li-S cell. In these conditions, excellent electrochemical performances were achieved with specific capacities that were either comparable to [44,45] (or surpassing [46,47]) recently reported values for other Si/C composites, conclusively confirming the versatile nature of CNS as scaffolds or matrices for different active materials in energy storage devices. On coupling such designed S/C cathodes with the lithiated Si@CNS-rGO anodes, a full cell is developed. After balancing the electrodes, the assembled full cell exhibited appreciating electrochemical performance with initial capacity of  $800 \text{ mAh/g}$  and  $40\%$  capacity retention over 100 cycles at  $0.1\text{C}$ .

## Results and Discussion

### Physicochemical characterization of S@CNS composite

The features of both CNS host and S@CNS composite are explored by a series of characterizations. By addition of 20 wt.% fumed  $\text{SiO}_2$  as a template agent during NS synthesis and after pyrolysis followed by  $\text{SiO}_2$  removal, the porous carbon shows a micro/meso-porosity. Figure 1 depicts the  $\text{N}_2$  adsorption/desorption isotherms of CNS obtained by template method.

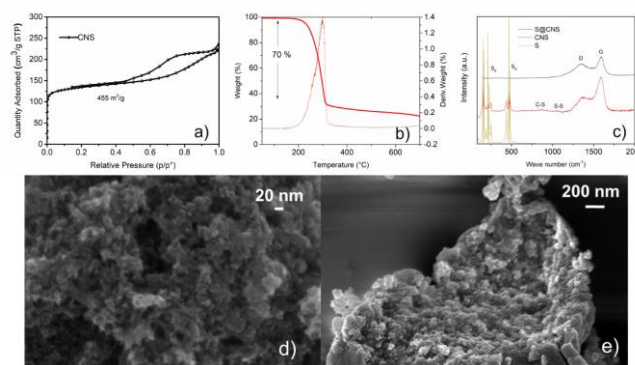


**Figure 1.**  $\text{N}_2$  adsorption/desorption isotherms of CNS (a), TGA analysis of S@CNS (b), Raman analysis of elemental sulphur, S@CNS, CNS (c), FESEM analysis of CNS (d), FESEM analysis of S@CNS (e).

The first steep increase at low relative pressure is related to adsorption in micro-pores, then the hysteresis loop is typical of IV type isotherm due to meso-pores. The porosity of CNS is formed

## FULL PAPER

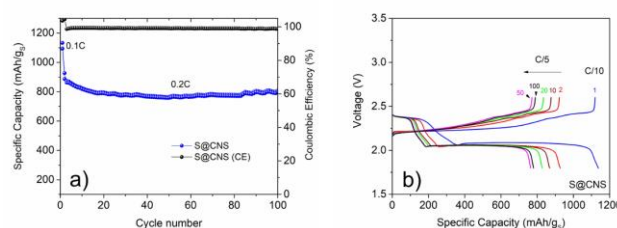
by two well-defined pore systems: uniform micro-pores ( $\approx 0.5$ – $2.0$  nm) and meso-pores ( $\approx 3.0$ – $10$  nm), with cumulative pore volume of  $0.35 \text{ cm}^3 \text{ g}^{-1}$  and BET surface area of  $455 \text{ m}^2 \text{ g}^{-1}$ . The CNS was then used to host sulfur, which was infiltrated by melt diffusion to obtain the S@CNS composite. TGA analysis shows that 70 wt.% of sulfur is incorporated in S@CNS (Figure 1b). Raman spectroscopy was performed for sulfur, CNS and S@CNS (Figure 1c). The characteristic peaks of elemental sulphur are sharp in the Raman spectrum of S@CNS, [48] indicating its crystalline nature [49]. S@CNS shows distinctive peaks at  $814$  and  $1070 \text{ cm}^{-1}$  that, based on previous reports [50], correspond to C–S and S–S stretch modes, respectively. Raman spectra also show two major peaks at  $1347$  and  $1589 \text{ cm}^{-1}$  typical of carbonaceous materials, corresponding to the disorder-induced D band ( $A_{1g}$  mode) and the graphitic G band ( $E_{2g}$  mode), respectively. From the intensity ratio ( $I_D/I_G$ ), a value of  $\approx 0.89$  was calculated, representing moderate degree of graphitization of CNS. After sulfur infiltration, the  $I_D/I_G$  ratio decreased and this was ascribed to the interaction of sulfur with the functional groups on the CNS surface (carbonyl, carboxyl and C=C groups), which reduces the disorder degree of the carbon. [51]

Figure 1d,e shows the morphological features of CNS and S@CNS obtained by FESEM analysis. The CNS carbon shows a porous sponge-like structure, which consists of numerous regular and interconnected particles. After sulfur melt infusion, the morphology of S@CNS retains the pristine CNS structure (Figure 1e).

The XPS survey spectra (Figure 1Sa, Supporting Information) of CNS and S@CNS show that CNS is mainly composed of carbon (87.5 at.%) and oxygen (10.5 at.%), confirming the successful removal of  $\text{SiO}_2$  from the sample and traces of fluorine are the consequence of the HF treatment from template removal. After sulfur incorporation to obtain S@CNS, peaks at  $226 \text{ eV}$  and  $162 \text{ eV}$  are ascribed to  $\text{S}_{2s}$  and  $\text{S}_{2p}$ . Figure 1Sb shows the high resolution  $\text{C}_{1s}$  spectrum of CNS, which is deconvoluted into four contributions. The first peak is ascribed to the signals of  $\text{sp}^2$  and  $\text{sp}^3$  of C–C and C=C bonds ( $284.7 \text{ eV}$ ). The other three contributions are centred at  $285.7$ ,  $287.5$  and  $289.5 \text{ eV}$ , corresponding to hydroxyl/epoxy (C–O), carbonyl (C=O) and carboxyl ( $-\text{O}-\text{C}=\text{O}$ ) groups, respectively. The deconvoluted  $\text{C}_{1s}$  spectrum of S@CNS (Figure 1Sc) shows larger contribution of the peak at  $285.7 \text{ eV}$  (62.25% for S@CNS, 17.16% for CNS), that can be assigned to both C–O and C–S, since they fall in the same range of binding energies ( $286 \text{ eV}$ ), [52] suggesting that sulphur is bonded to the CNS. This is consistent with the decrease of the peak of C=O in S@CNS (4.1%) with respect to CNS (6.8%). Figure 1Sd in Supporting Information shows the  $\text{S}_{2p}$  high resolution spectra of S@CNS, which is characteristic of sulfur in the carbon host. [53] Oxidized sulfur appears at binding energy of  $167.0 \text{ eV}$ .

### Electrochemistry of the S@CNS composite cathode

Long-term cycling performance of Li-S cells are evaluated (Figure 2) in the voltage range of  $1.8$ – $2.6 \text{ V}$  vs.  $\text{Li/Li}^+$  in DOL/DME/ $\text{LiNO}_3$ ; all the capacity values are calculated on the weight of sulfur in the cathode.



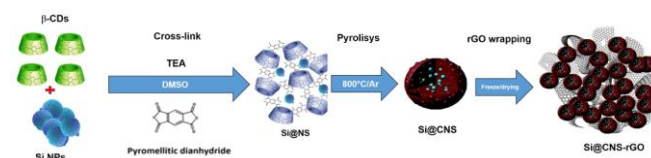
**Figure 2.** Capacity vs. cycle number of S@CNS cell: first cycle at  $0.1\text{C}$  followed by cycling at  $0.2\text{C}$  (a), voltage vs. capacity plot of S@CNS at  $0.2\text{C}$  (b).

As observed in Figure 2a, the first discharge capacity at  $0.1\text{C}$  is about  $1135 \text{ mAh g}^{-1}$ , which is 67.6% of the theoretical capacity of sulfur. The Coulombic efficiency (CE) at the 1<sup>st</sup> cycle is 103%, characterized by moderate overcharge due to parasitic reactions, but from the 6<sup>th</sup> cycle onwards at  $0.2\text{C}$ , the CE is stabilized at 99%. At  $0.2\text{C}$  rate, the S@CNS cathode (Figure 2a) shows very stable cycling performance from the early cycles. An initial capacity of  $927 \text{ mAh g}^{-1}$  is observed with capacity retention of 85% over 100 cycles, demonstrating very good cycling stability.

Figure 2S (Supporting Information) shows the  $dQ/dV$  profiles, in which the  $D_1$  peak, centred at  $2.3 \text{ V}$ , reflects overlapped formation processes due to series of reduction reactions from  $\text{S}_8$  to  $\text{Li}_2\text{S}_n$ ,  $4 \leq n \leq 8$ . The  $D_2$  peak at  $2.0 \text{ V}$  corresponds to the further reduction from  $\text{Li}_2\text{S}_n$  to  $\text{Li}_2\text{S}$ . The small peak at  $2.1 \text{ V}$  could be related to intermediate species produced during redox process that presumably involves disproportionation reactions. [54] In the charge process of S@CNS cell, three peaks of different intensity ( $C_1$ – $C_3$ ) in the  $dQ/dV$  curves are distinguished (Figure 2S in Supporting Information) [55], which are referred to a charge mechanism that implies the multistep oxidation to sulphur [56]. From the 2<sup>nd</sup> to the 100<sup>th</sup> cycle, the  $C_1$ – $C_3$  peaks do not disappear and their position is only slightly shifted over cycling, confirming the good electrochemical stability of the S@CNS composite due to the ability of CNS to confine the polysulphides.

### Physicochemical characterization of Si@CNS-rGO composite

For the Si anode, we propose an integrated strategy, which again exploits the carbonized ester-CDNS synthesized through PMDA crosslinking [57] as excellent supports to anchor Si NPs. As depicted in the sketch of Scheme 1, the first step of the Si@CNS-rGO synthesis involves the crosslinking of CDs to obtain the NS, in which Si NPs are directly embedded.



**Scheme 1.** Schematic representation of the multi-step synthesis of Si@CNS-rGO.



## FULL PAPER

A brownish gel is formed after the addition of PMDA and TEA catalyst. Pyrolysis of Si@NS composite at 800 °C in inert atmosphere results in Si@CNS material. Further wrapping with rGO produces the Si@CNS-rGO composite, in which rGO improves the electrical conductivity of the material. Morphological characterization of Si@CNS through FESEM imaging reveals that the spherical Si NPs are anchored to the surface of CNS (Figure 3a). Layers of rGO completely wrap the Si@CNS in the Si@CNS-rGO composite (Figure 3b). TEM images of Si@CNS-rGO (Figure 3c-d) enlighten the Si NPs on CNS and the rGO layers, as above observed. Energy-dispersive X-ray spectroscopy (EDS) mapping on the spherical particles indicates that Si NPs are covered by amorphous SiO<sub>2</sub>, which is consistent with the commercial Tekmat™ Si-N100 nanopowder used in this work (Figure 3e). Some Si NPs are completely embedded in the CNS, as shown by the STEM image of Figure 3f and the stiff carbon framework could function as a cage to hold the pulverized silicon pieces.

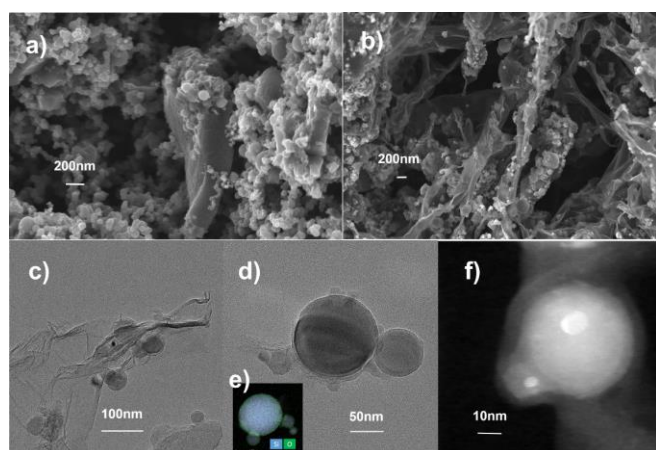


**Figure 3.** FESEM micrographies of Si@CNS (a) and of Si@CNS-rGO (b), TEM micrographies of Si@CNS-rGO (c,d), EDS mapping on a spherical silicon nanoparticle (e), STEM image of a Si nanoparticle (f).

XRD analysis of the composite is depicted in Figure 3Sa (Supporting Information) and shows contributions from both carbon and crystalline silicon. Typical diffraction pattern arising from cubic crystal structure of silicon is observed (ICSD 98-004-1979) and a broad halo comes from the carbon (*i.e.*,  $2\theta \sim 24^\circ$ ). TGA analysis of the Si@CNS-rGO (Figure 3Sb) was performed in air until 800 °C. The oxidation of carbon around 550 °C results in solid content of about 35.85 wt.%, that corresponds to silicon. Rising the temperature beyond 700 °C comes up with increase of solid content, which is related to the oxidation of Si. The N<sub>2</sub> adsorption isotherm of both Si@CNS and CNS materials show type I isotherms in the IUPAC classification, that are typical of microporous materials (Figure 3Sc). The first steep increase at low relative pressure is related to adsorption in micropores, the second step is fairly constant, followed by the condensation in the micropores. The Si@CNS has a BET surface area of 431 m<sup>2</sup> g<sup>-1</sup>. Compared to CNS, the Si@CNS material adsorbed less N<sub>2</sub>. This result points out that pores are occupied by Si NPs inside the CNS. The BET surface area reduction from CNS to Si@CNS (from 560 to 431 m<sup>2</sup> g<sup>-1</sup>) indicates the successful insertion of Si NPs into carbon. The presence of porosity is important to guarantee good

ionic conductivity of well-impregnated silicon particles with the electrolyte, as well as to provide sufficient void space during lithiation and delithiation for expansion and shrinking of the spherical nanoparticles.

To observe the phase characteristics of Si@CNS, the XPS analysis of the composite was performed (Figure 4S, Supporting Information). As expected, the survey spectrum of Si@CNS shows only O, C, Si as constituents of the composite. In the high-resolution C1s spectrum (Figure 4Sb), the main peak centred at 284.78 eV is due to graphitic sp<sup>2</sup> and to sp<sup>3</sup> carbon and the additional components at 285.6 and 288.9 eV are assigned to C–O and O–C=O, respectively, as previously observed for S@CNS composite (Figure 1Sb). The peak at 291.64 eV is consistent to the  $\pi$ – $\pi^*$  shake up satellite from the aromatic structure.<sup>[58]</sup> The presence of carbon double bonds and the aromatic structure in CNS results from the reaction path occurring in the pyrolysis of the nanosponge. During crosslinking of CD, PMDA experiences the ring opening reaction, which is followed by the formation of ester bridges.<sup>[34]</sup> The latter is the thermally weak bond in the pyrolysis step, allowing the extraction of a hydrogen atom from CD, resulting in the final graphitic structure of char.<sup>[38]</sup> In the high-resolution Si2p spectrum (Figure 4Sc), the elemental silicon is observed at 98.30 eV (Si<sub>2p 3/2</sub>) and 99.39 eV (Si<sub>2p 1/2</sub>), whereas the peak at 103.7 eV is assigned to Si–O<sub>x</sub> species (Si<sup>4+</sup>), indicating that nano-Si surface is partly oxidized. The peak at 102.1 eV is assigned to the formation of the Si–O–C bonds,<sup>[59]</sup> which confirms the anchoring of Si NPs to CNS. The high-resolution O1s XPS spectrum (Figure 4Sd) shows two components at 531.6 eV and 533.8 eV, that can be ascribed to Si–O–C<sup>[60]</sup> and Si–O–Si<sup>[61]</sup> bonds.

#### Electrochemistry of the Si@CNS-rGO composite anode

The benefits of r-GO wrapping the Si@CNS composite are verified by electrochemical tests. Figure 5S (Supporting Information) reports the specific capacity vs. cycle number of Si@CNS and Si@CNS-rGO cells at 0.1C in LP30 electrolyte. The Si@CNS shows an initial capacity of 2643 mAh g<sup>-1</sup>, similar to that of Si@CNS-rGO (2281 mAh g<sup>-1</sup>). These high capacity values indicate that both composite materials are electrically well connected and active in the electrochemical lithiation and delithiation reactions. However, the Si@CNS retains 51% of the initial capacity after 20 cycles, while stable cycling is observed for the Si@CNS-rGO cell. This way, r-GO layers behave as double-protection for Si NPs, either by providing conductive, porous and elastic network and by preventing aggregation and pulverization of Si NPs during charge/discharge processes. The low initial CE (58.4%) of Si@CNS-rGO may be due to side reactions with the electrolyte as a result of the surface area and/or functional groups of r-GO.<sup>[62]</sup> The Si@CNS-rGO was tested in ether-based electrolytes in order to check the suitability as anode for the sulfur cell. However, a comparison in typical Li-ion electrolytes was necessary to assess Si@CNS-rGO electrochemical performance and thus carried out. To this purpose, carbonate-based commercial LP30 (with or without FEC) and typical DOL/DME/LiTFSI (with or without LiNO<sub>3</sub>) electrolytes were employed in this work. Besides, we propose FEC additive as a viable alternative to LiNO<sub>3</sub> for silicon lithiation/delithiation in DOL/DME, for the well-known ability of FEC to increase both CE and cycling stability of silicon anodes. This is due to the composition of SEI layer, mainly of LiF and Li<sub>2</sub>O derived from FEC

## FULL PAPER

decomposition, which protects Si from cracking during cycling.<sup>[63]</sup> Moreover, with FEC addition, the Si surface is not entirely covered by inorganic species, but is partially bonded to the organic SEI that acts as  $\text{Li}^+$  conductor and forms an elastic film around Si NPs.<sup>[64]</sup> Figure 4 shows the lithiation capacity vs. number of cycles of Si@CNS-rGO at 0.1C in DOL/DME/FEC and in LP30, respectively. As can be seen, Si@CNS-rGO shows high capacity values in all the electrolytes, but differences are seen in the capacity retention during cycling. In DOL/DME/FEC, from the 2<sup>nd</sup> cycle onwards, the lithiation capacity of Si@CNS-rGO is about 3200 mAh  $\text{g}_{\text{Si}}^{-1}$ , which is 89% of silicon theoretical capacity. Taking into account the total mass of active material on the electrode and subtracting the contribution to the capacity of CNS, the lithiation capacity is still 2299 mAh  $\text{g}^{-1}$ , which is 64% of the theoretic value, highlighting the good electrochemical performance of Si@CNS-rGO.

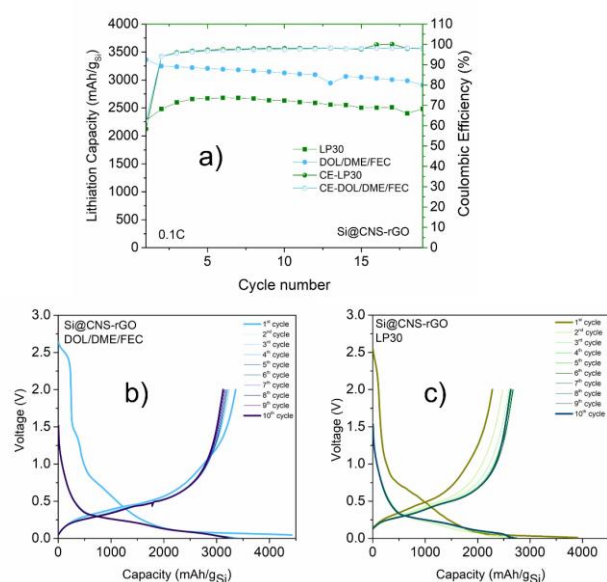


**Figure 4.** Evolution of the lithiation capacity vs. number of cycles of Si@CNS-rGO in DOL/DME/FEC and in LP30 at 0.1C (a), voltage vs. capacity plots at 0.1C in: (b) LP30 and (c) in DOL/DME/FEC.

However, in LP30, the lithiation capacity is far less (2281 mAh  $\text{g}^{-1}$ ) and the slight increase initially observed can be assigned to a continuous material activation as a result of a delayed infiltration of the electrolyte in the Si@CNS-rGO structure, which probably limits the initial level of lithiation attained in this electrolyte, even at low C rates.<sup>[65]</sup> More specifically, Jaumann *et al.*<sup>[66]</sup> suggested that full utilization of silicon is not achieved in LP30, while ether-based electrolytes promote silicon lithiation from the early cycles. This entails a more resistive SEI film is formed on Si@CNS-rGO in LP30, which slows down the Li-Si alloying kinetics.<sup>[67]</sup> In DOL/DME/FEC, the CE value is 62.3% at the 1<sup>st</sup> cycle, consistent with the assumption of higher reversibility. From the 10<sup>th</sup> cycle onwards, the CE of Si@CNS-rGO approaches 98%, indicating a stable SEI layer is formed. Figure 4b,c shows the voltage vs. capacity curves of Si@CNS-rGO. During the 1<sup>st</sup> lithiation, a flat voltage plateau at 1.45 V vs.  $\text{Li}/\text{Li}^+$  appears in DOL/DME/FEC, while in LP30 the slope below 0.8 V vs.  $\text{Li}/\text{Li}^+$  is due to the decomposition of EC. Differential capacity-voltage plots ( $\text{dQ}/\text{dV}$ )

better document this reduction (Figure 6S in Supporting Information). The peaks at the 1<sup>st</sup> cycle show the potentials at which the electrolyte is reduced. In LP30, the reduction starts at about 1.0 V with a cathodic maximum about 0.67 V, which disappears at the 2<sup>nd</sup> cycle. This is attributed to electrolyte decomposition and SEI formation.<sup>[68]</sup> In DOL/DME/FEC, the peak at 1.4 V is assigned to FEC reduction<sup>[69]</sup> on Si@CNS-rGO, which appears prior to the electrolyte solvent reduction (at about 1.2 V for DOL/DME), implying that FEC-derived SEI layer mitigates the parasitic reactions by severing silicon from direct exposure to the electrolyte. At the 1<sup>st</sup> cycle, the lithiation of Si@CNS-rGO occurs at potentials lower than 0.1 V, which is depicted by the sharp peak in the  $\text{dQ}/\text{dV}$  profiles.<sup>[70]</sup> First delithiation in both electrolytes directly proceeds through two peaks located at around 0.28 V and 0.45 V. These double humped features indicate amorphization of Si-CNS@r-GO, due to the small size of silicon nanoparticles. The similar profiles in the different electrolytes suggest that silicon undergoes the same redox processes irrespective from the nature of the electrolyte.<sup>[71]</sup> However, in DOL/DME/FEC the pronounced anodic peak centred at 0.45 V is a sign of larger electrochemical activity,<sup>[72]</sup> consistent with lower impedance as discussed hereafter.<sup>[73]</sup> Lithiation beyond the 1<sup>st</sup> cycle also comprises peaks at 0.25 V and 0.1 V that are related to the stepwise-lithium insertion into amorphous silicon to form amorphous  $\text{Li}_x\text{Si}$ . The stability of the  $\text{dQ}/\text{dV}$  features results from the stable microstructure of Si-CNS@r-GO, since no noticeable change is observed during cycling. The same trend of silicon lithiation/delithiation through amorphous  $\text{Li}_x\text{Si}$  is confirmed by the cyclic voltammetry (CV) shown in Figure 7Sa (Supporting information). As a comparison, the CV of CNS carbon is also reported (Figure 7Sb). The overall reversible capacity of the bare CNS scaffold is 140 mAh  $\text{g}^{-1}$  in DOL/DME/FEC (Figure 7c). Increasing the C-rate of the reaction, the electrochemical behaviour of Si@CNS-rGO is dependent on the initial level of lithiation attained and on the SEI layer formed.

To demonstrate this, the Si@CNS-rGO was initially lithiated/delithiated at 0.1C for one cycle, followed by 100 cycles at 1C. Tests were carried out either in LP30 and in DOL/DME with or without  $\text{LiNO}_3$  and FEC additives. As depicted in Figure 5a, with FEC additive the cell experiences higher capacity retention and cycling stability in both carbonate-based and ether-based electrolytes. In DOL/DME, the initial lithiation capacity of Si@CNS-rGO is the highest (2516 mAh  $\text{g}_{\text{Si}}^{-1}$ ), suggesting that Si@CNS-rGO is a potentially excellent anode for the sulphur battery.

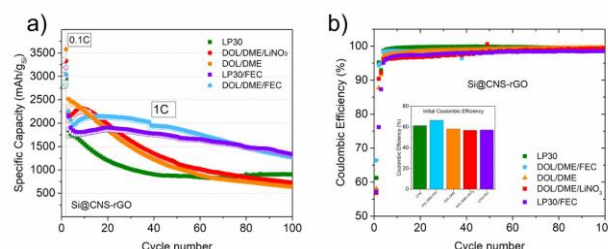


**Figure 5.** Capacity vs. number of cycles curves of Si@CNS-rGO in the different electrolytes at 1C (a), CE (b).

The addition of FEC and  $\text{LiNO}_3$  increases the reversibility and the capacity retention, but decreases the initial capacity of 10–12%



## FULL PAPER

with respect to DOL/DME, due to the higher electrolyte resistance (higher viscosity) with additives. [66] Without FEC, the Si@CNS-rGO suffers more capacity fading in LP30 and the initial lithiation capacity is 21% lower than that in DOL/DME, in agreement with previous findings. [67] At 0.1C, the CE values are 66% in DOL/DME/FEC, 63% in LP30, 60% in DOL/DME, 57% in LP30:FEC and 56% DOL/DME/LiNO<sub>3</sub> (Figure 5b). The lower initial CE with LiNO<sub>3</sub> suggests higher electrolyte consumption compared to the additive-free electrolyte. The dQ/dV plots (Figure 8S Supporting Information) display a large reduction peak at 1.6 V vs. Li/Li<sup>+</sup>, which is not observed in LiNO<sub>3</sub>-free DOL/DME and consistent with previous reports. [66] In DOL/DME/FEC, the lithiation capacity is 1283 mAh g<sub>Si</sub><sup>-1</sup>, representing a 56% capacity retention over 100 cycles, with more than 98.5% CE (Figure 5a,b). The analysis of the dQ/dV plots vs. cycle number (Figure 9S Supporting Information) shows how the electrochemical potentials (for lithiation/delithiation of Si@CNS-rGO) shift with increasing cycle number in all electrolytes, except those with FEC. This increase in the voltage hysteresis between lithiation and delithiation as the cycles progress is an indication of the continuously growing SEI layer on the silicon surface. [71]

In LP30, the hysteresis is so large that could indicate incomplete lithiation as the major fading mechanism, due to the formation of more resistive and rigid SEI [67] that can further enhance the cracking of Si. Electrochemical impedance spectroscopy, Figure 10S in Supporting Information, shows that the value of charge transfer resistance ( $R_c$ ) dominates the kinetics of the electrode reactions in LP30 and the  $R_{SEI}$ , attributed to Li<sup>+</sup> migration in the surface film, is high that implies a thick or poorly conductive SEI layer is formed. After lithiation/delithiation, the  $R_c$  is reduced due to the amorphization of crystalline silicon. [74] A further proof of incomplete lithiation in LP30 due to high impedance is shown in Figure 10Sc (Supporting Information), that depicts the XRD analysis of the electrodes after 100 cycles at 1C compared to that of pristine Si@CNS-rGO. As seen, the amount of crystalline silicon in LP30 is higher than that in DOL/DME/FEC. It means that a lower amount of silicon is transformed into amorphous phase. On the contrary, very small amount of crystalline silicon exists in the electrode cycled in DOL/DME/FEC. The additional peaks appearing in XRD pattern are assigned to LiF (ICSD 98-001-8012, PDF code 00-004-0857), consistent to FEC decomposition. For this reason, FEC additive is mandatory to achieve stable cycling in both electrolytes.

Finally, it is worth noting that the lithiation capacity increases of about 35% if the cell experiences 24 h rest in DOL/DME/FEC before galvanostatic cycling (Figure 11S Supporting Information). This is a result of the delayed infiltration of the electrolyte in the porous Si@CNS-rGO structure. This procedure allows higher silicon utilization as a consequence of well-impregnated silicon particles with the electrolyte. However, the behaviour of Si@CNS-rGO remains unchanged. As seen, the initial CE value is about 65% (as previously observed) and the differential capacity-voltage plots (Figure 11Sb) show the same trend for lithiation/delithiation of silicon; the latter are also in agreement with previously reported works that associated such dQ/dV trend with amorphous to crystalline phase transformation in Li-rich Li<sub>x</sub>Si phases. [75]

## Full cell: lithiated Si@CNS-rGO anode vs. S@CNS cathode

To demonstrate the feasibility of designing individual electrodes, a lithiated Si-S full cell was assembled using lithiated Si@CNS-rGO anode and S@CNS cathode (Si@CNS-rGO | S@CNS). For the purpose, the Si@CNS-rGO pre-lithiation was carried out DOL/DME and in DOL/DME/FEC electrolytes, respectively. The Si@CNS-rGO | S@CNS shows the characteristic capacity vs. voltage profiles (Figure 6) that can be attributed to the optimization of both cathode and anode for the lithiated Si-S cells for the development of low-cost energy storage systems. An initial discharge capacity of 800 mAh g<sub>s</sub><sup>-1</sup> is achieved for Si@CNS-rGO | S@CNS and the capacity of 215 mAh g<sub>s</sub><sup>-1</sup> is retained after 200 cycles, consistent with the electrochemical behavior of similar lithiated Si-S cell prototypes. [76–78]

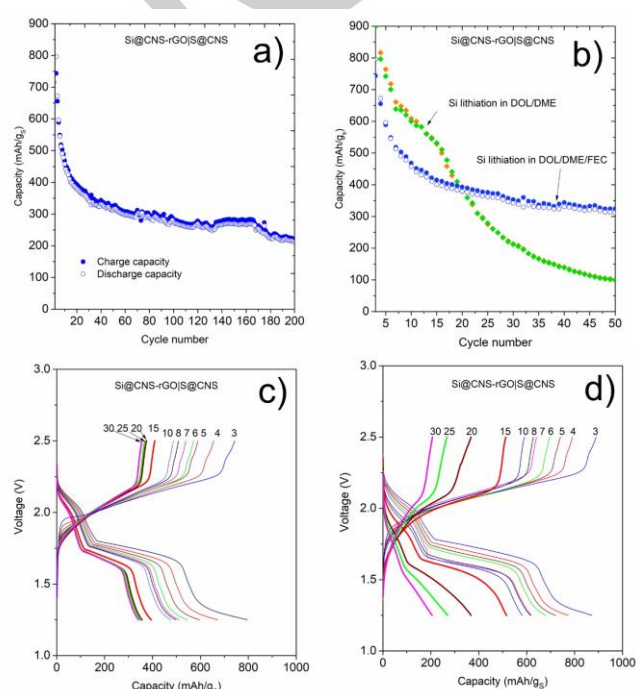


**Figure 6.** Capacity vs. number of cycles curves of Si@CNS-rGO | S@CNS full cell at 0.1 C: Si@CNS-rGO prelithiation in DOL/DME/FEC (a), Si@CNS-rGO prelithiation in DOL/DME/FEC and in DOL/DME (50 cycles) (b). Voltage vs. capacity curves of the Si@CNS-rGO | S@CNS full cell at 0.1 C: Si@CNS-rGO prelithiation in DOL/DME/FEC (c), Si@CNS-rGO prelithiation in DOL/DME (d).

The 1<sup>st</sup> and 2<sup>nd</sup> discharge plateaus at 2.1 and 1.7 V respectively, are lower than those of the Li-S@CNS half-cell due to the increasing de-lithiation potential of Si@CNS-rGO anode. The prelithiated Si electrode is more active than metallic lithium in polysulfide reactions due to the larger specific surface area of lithiated Si NPs. Moreover, decomposition of LiNO<sub>3</sub> can aggravate the side reactions especially in the initial cycles. For these reasons, the Si@CNS-rGO | S@CNS full cell displays lower capacity values than that of Li-S@CNS half-cell. Future work will be directed to develop interlayers to cope active materials losses in the initial cycles. It is worth noting, as shown in Figure 6b, that the selection of the electrolyte for silicon pre-lithiation plays an important role on the electrochemical performance of the final full

## FULL PAPER

cell. The Si@CNS-rGO | S@CNS cell, with Si pre-lithiated in DOL/DME, experiences a capacity loss of 76.5% after 30 cycles (Figure 6b,d), consistent with the trend previously observed in this electrolyte. On the contrary, Si pre-lithiation with FEC additive optimizes the anode/electrolyte interface and assures better cycling stability of the Si@CNS-rGO | S@CNS full cell, because Si@CNS-rGO can benefit the formation of a thin, dense SEI that protects the electrode during cell cycling. This recovery ability demonstrates that the lithiated Si-S cell can successfully maintain a certain structural integrity under long cycling, in which the operation conditions are severe (low C rates) due to the extent of LiPSs shuttling.

## Conclusions

In summary, novel carbons derived from bio-based NS to host sulfur and silicon nanoparticles have been proposed for the fabrication of high capacity electrodes, with the potential to be used in lithiated Si-S cells, exploiting the advantage of having a common carbon matrix for both. For the first time it was successfully demonstrated that the template method is suitable to create meso-pores in the nanosponge and this spongy structure makes the carbon absorptive for sulphur. The overall CNS synthesis is easy to scale-up and forecasts new strategies for meso-porous carbon preparation. At 0.2C, the initial cell capacity is 927 mAh g<sup>-1</sup> and good capacity retention of 85% is achieved over 100 cycles, demonstrating good cycling stability. Moreover, micro-porous CNS have proved to be excellent supports for silicon, in which Si NPs are directly embedded in the CNS. Further wrapping with rGO provides suitable conductive network to the composite. We have demonstrated the feasibility of the Si@CNS-rGO to be coupled with typical ether-based electrolytes of the sulphur battery and best performances were achieved by addition of 5 wt.% FEC as an additive. By using the proposed strategy, cells were able to deliver 2000 mAh g<sub>Si</sub><sup>-1</sup> at 1C with capacity loss of 0.4% per cycle for 100 cycles. Introduction of a rest time of 24 h raised the cell capacity to 2500 mAh g<sub>Si</sub><sup>-1</sup> at 1C with capacity retention of 68% for 100 cycles. Coupling such S@CNS cathodes with the lithiated Si@CNS-rGO anodes leads to the realization of lithiated Si-S full cell. After balancing the electrodes, the assembled lithiated silicon-sulfur cell exhibited appreciating electrochemical performance with initial capacity of 800 mAh g<sup>-1</sup> at 0.1C with 30% capacity retention over 200 cycles. Future development of suitable interlayers could alleviate the capacity fade in the early cycles. This work demonstrates a step forward towards the integration of silicon anodes and SEI manipulation into sulphur cells for high energy applications.

## Experimental Section

### Materials Preparation

*Synthesis of micro/meso-porous carbons from CD-NS crosslinked with pyromellitic dianhydrides:* Polymerization of CD is the method to form NS. To this purpose, a sol-gel process was carried out to form an organogel. The method consisted in dissolving the CD (Roquette Italia SpA, Italy), dimethylsulfoxide (DMSO, Aldrich), followed by addition of a catalyst and

a cross-linker. In this case, the cross-linking agent was the pyromellitic dianhydride (benzene-1,2,4,5-tetracarboxylic dianhydride, PMDA, Aldrich) in the molar ratio CD:PMDA 1:4. Once the product formed, NS were washed, to remove all impurities and unreacted CD, and finally dried. To obtain mesoporous carbonized nanosponges (CNS), silica fumed powder with average particles size of 7 nm was used as a template to prepare the precursor NS. The highest amount of SiO<sub>2</sub> (Aldrich) that could be introduced in the NS structure, without negatively impacting the gelation step and therefore allowing NS formation, was 20 wt.%. To this purpose, 2.0 g of silica were dispersed in 25 mL of DMSO and kept under continuous sonication. To this dispersion, 4.56 g of anhydrous CD were added under stirring until their complete dissolution was achieved. Following the addition of 5 mL of triethylamine (TEA, Aldrich) catalyst and 3.44 g of PMDA, the gelation was completed at room temperature within 15 min. The obtained product was purified by washing several times, dried and grounded. SiO<sub>2</sub> removal was achieved with hydrofluoric acid (HF, Aldrich). After silica removal, the CNS were washed several times with deionized water and vacuum dried.

*Preparation of S@CNS active material for sulphur cathode:* The CNS were used to prepare S@CNS composite. The solution impregnation method was performed by dissolution of 3.0 g sulfur powder (Aldrich) in 10 mL carbon disulfide (CS<sub>2</sub>, Aldrich) in a sealed reactor. Then, 1.0 g of CNS was added to the mixture and stirred until complete evaporation of the solvent. For infiltration of sulfur inside the carbon pores, the dried sample was heated to 155 °C for 10 h in argon atmosphere with a heating ramp of 1.0 °C/min to guarantee the penetration of sulfur in the micro/meso-pores. The sample was cooled naturally to trap the crystallized sulphur in the pores.

*Synthesis of Si@CNS composites as anode active material:* The Si NPs used in this work were purchased from Aldrich (Tekmat™ Si-N100 nanopowder <100 nm, <3% oxygen passivation). To synthesize Si@NS, 1 g of Si NPs was dispersed in 10 mL DMSO and sonicated for 2 h. Then, CD (2.25 g), TEA (2.0 ml) and PMDA (1.74 g) were successively added as previously described. Once the reaction was complete with gel formation, the sample was washed several times with distilled water and acetone (Aldrich). The Si@NS, contained in a Coors combustion boat, was introduced in a Lenton tubular furnace and heated at 800 °C with a heating ramp of 10 °C min<sup>-1</sup> under N<sub>2</sub> flow (100 mL min<sup>-1</sup>) to obtain Si@CNS composite.

*Synthesis of graphene wrapped silicon anode: Si@CNS-rGO:* The Si@CNS composite was wrapped by rGO layers. The first step consisted in homogeneous mixing of the milled Si@CNS with a graphene oxide (GO, Graphenea) suspension, by both magnetic stirring and sonication. In detail, 400 mg of Si@CNS powder were dispersed in 100 mL of deionized water in a round bottom flask and sonicated for 2 h. Then, addition of 25 mL of GO dispersion and sonication for 2 h were carried out. The flask was quickly introduced in a nitrogen dewar and subsequently connected to freeze-dryer system at -50 °C for 48 h. After drying, the sample was introduced in a tubular oven in H<sub>2</sub>/Ar flow (3% of H<sub>2</sub>) at 800 °C to reduce GO, at a heating ramp of 10 °C min<sup>-1</sup>.

### Materials characterization

FESEM (Field Emission Scanning Electron Microscope) analysis was carried out by Zeiss SUPRA™ 40 with Gemini column and Schottky field emission tip (tungsten at 1800 K). Acquisitions were made at acceleration voltage of 3 kV and working distance (WD) between 2.1 and 8.5 mm, with magnification up to 1000 kX. The scanning/transmission electron microscope (S/TEM) analysis was carried out using a Thermo Scientific™ Talos F200X. X-ray photoelectron spectroscopy (XPS) measurements were carried out using a PHI Model 5000 electron spectrometer equipped with an aluminium anode (1486 eV) monochromatic source, with a power

## FULL PAPER

of 25.0 W, and high-resolution scan with 11.75 eV pass energy. The instrument typically operates at pressures below  $5 \times 10^{-8}$  mbar.

The Brunauer-Emmett-Teller (BET) specific surface area (SSA) was determined by  $N_2$  physisorption at 77 K using a Micrometrics ASAP 2020 instrument. The SSA was calculated with the BET model in the relative pressure range of 0.07–0.30 by assuming  $0.162 \text{ nm}^2 \text{ molecule}^{-1}$  as the molecular area of  $N_2$ .

The X-rays diffraction (XRD) patterns were recorded by Panalytical X'Pert PRO diffractometer with a PIXcel detector, using Cu K $\alpha$  radiation, under the conditions of  $2\theta = 10\text{--}100^\circ$  and  $2\theta$  step size = 0.03.

Thermogravimetric analyses (TGA) were carried out on a Mettler Toledo TGA/SDTA 851 instrument by heating the composite at  $10^\circ \text{C min}^{-1}$  from room temperature to  $800^\circ \text{C}$  under air (in the case of silicon composite) or under  $N_2$  (in the case of sulfur composite).

Raman spectroscopy of sulfur, CNS and S@CNS was carried out on Renishaw InVia micro-Raman spectrometer, with a laser excitation wavelength of 514.5 nm and a laser spot size of  $\sim 20 \mu\text{m}$ .

### Cell assembly and electrochemical measurements

For the half-cell testing of individual electrodes, coin cells (CR2032 type) were assembled in Ar-filled dry glove box (Mbraun Labstar with  $O_2$  and  $H_2O < 0.1$  ppm) using lithium metal as anode (lithium disc  $16 \times 0.2$  mm, Chemetall s.r.l.). For the cathode, S@CNS (80%) was mixed with 10 % carbon black (TIMICAL Super C65) and 10% PVDF in NMP. The slurry was mixed by mixer mill (MM400, Retsch) at 20 Hz for 20 min. All slurries were casted on Al foil using doctor blade with clearance around  $200 \mu\text{m}$  by automatic film applicator. The slurries were dried at room temperature and 15 mm diameter cathodes were punched out. The cathodes were shifted to argon glove box after 4 h drying at  $50^\circ \text{C}$  under vacuum. The sulfur loading was about  $1.2 \text{ mg cm}^{-2}$ . Celgard 2500 soaked with the electrolyte was used as separator. For the sulphur cell, the standard electrolyte consisted of 1,2-dimethoxyethane (DME, Aldrich) and 1,3-dioxolane (DOL, Aldrich) 1:1 (v/v) with 1 M Lithium bis(trifluoromethanesulfonyl)imide  $LiC_2F_5NO_4S_2$ , LiTFSI Solvionic) and 0.25 M  $LiNO_3$  (Aldrich). Each cell contained no more than  $20 \mu\text{L}$  of electrolyte. Cells comprising sulfur cathodes were galvanostatically discharged to 1.8 V and charged to 2.6 V by an Arbin BT-2000 battery tester at room temperature. The C-rate was calculated using the theoretical capacity of sulfur (i.e.,  $1672 \text{ mAh g}^{-1}$ ). For Si@CNS-rGO anodes, the working electrodes were prepared by solvent tape casting method. An aqueous based slurry of the as-prepared Si@CNS-rGO sample was mixed with sodium alginate binder and C45 in the weight ratio of 70:10:20. The slurry was mechanically deposited on the copper current collector by doctor blade technique. The blade was adjusted for  $150 \mu\text{m}$  deposition using an automatic film applicator (Sheen 1133 N) with a speed of  $50 \text{ mm s}^{-1}$ . After solvent evaporation in air, disks of  $1.76 \text{ cm}^2$  were punched out, vacuum dried at  $120^\circ \text{C}$  (Büchi Glass Oven B-585) for 4 h and assembled in the coin cell with lithium metal inside the glove-box. The mass loading of silicon was in the range of  $0.55\text{--}0.58 \text{ mg cm}^{-2}$  in each electrode. The composition of the electrolytes used in this work is the following: i) LP30: 1.0 M of lithium hexafluorophosphate ( $LiPF_6$ ) in 1:1 (v/v) mixture of ethylene carbonate (EC) and diethyl carbonate (DEC) (battery grade, Solvionic); ii) DOL/DME: 1 M LiTFSI in 1:1 (v/v) mixture of DME and DOL; iii) DOL/DME/FEC: 1 M LiTFSI + 5 wt.% FEC in 1:1 (v/v) mixture of DME and DOL; iv) LP30/FEC: 1.0 M of lithium hexafluorophosphate ( $LiPF_6$ ) in 1:1 (v/v) mixture of ethylene carbonate (EC) and diethyl carbonate (DEC) + 5 wt.% FEC. The amount of electrolyte in each cell was  $100 \mu\text{L}$ . Cells comprising Si@CNS-rGO were galvanostatically discharged to 0.01 V and charged to 2.0 V, C-rates are calculated using the theoretical capacity of silicon, which corresponds to  $3579 \text{ mAh g}^{-1}$ . For the purpose of pre-lithiation silicon anodes, an ECC-STD electrochemical cell

configuration (EL-Cell, GmbH) was employed. Lithiation of silicon was carried out using constant current constant voltage (CCCV) protocol in either DOL/DME/FEC and DOL/DME electrolytes. Discharging of half-cell was carried out at C/20 followed by holding voltage at 10 mV until constant current reached, then charging was performed at C/20 till until 2 V. This procedure was repeated five times. The Li $_x$ Si anode was reclaimed from EL cell set up in glove box. The anode was immersed in  $200 \mu\text{L}$  of DME for 5 s and this procedure was repeated three times with fresh DME, in the glove box. The full cell was assembled after balancing the active material amount of sulfur and silicon at the cathode and anode, respectively. Since in practice, silicon delithiation is incomplete due to SEI formation, the amount of silicon had to exceed the stoichiometric one with respect to S mass thus, the Si/S weight ratio was set at 1.2. Then, the anode was used to assemble the full cell against sulfur cathodes in coin cell configuration. DOL/DME/ $LiNO_3$  electrolyte was employed in the full cell, in the amount of  $20 \mu\text{L}$  to ensure the wetting of all three components (i.e. sulfur cathode, silicon anode and separator). The full cells were subjected to charge and discharge between 1.1 and 2.5 V at current rate of C/10 based on mass of sulfur in cathodes.

### Acknowledgements

The research centre Y-TEC (YPF Tecnología S.A.) of Berisso (Buenos Aires, Argentina) is acknowledged for TEM analysis.

**Keywords:** nano-Si@carbon • S cathode • carbon nanosponges • cyclodextrin • reduced graphene oxide • Lithiated Si-S battery • Li-S battery • electrochemistry

- [1] J.-M. Tarascon, M. Armand, *Nature* **2001**, 414, 359–367.
- [2] P. G. Bruce, S. A. Freunberger, L. J. Hardwick, J.-M. Tarascon, *Nat. Mater.* **2012**, 11, 19–29.
- [3] G. Ganas, G. Kastrinaki, D. Zarvalis, G. Karagiannakis, A. G. Konstandopoulos, D. Versaci, S. Bodoardo, *Mater. Today Proc.* **2018**, 5, 27416–27424.
- [4] B. Dunn, H. Kamath, J.-M. Tarascon, *Science* **2011**, 334, 928–35.
- [5] Y.-T. Liu, D.-D. Han, L. Wang, G.-R. Li, S. Liu, X.-P. Gao, *Adv. Energy Mater.* **2019**, 9, 1803477.
- [6] N. P. Wagner, A. Tron, J. R. Tolchard, G. Noia, M. P. Bellmann, *J. Power Sources* **2019**, 414, 486–494.
- [7] C. de las Casas, W. Li, *J. Power Sources* **2012**, 208, 74–85.
- [8] F. Li, Q. Liu, J. Hu, Y. Feng, P. He, J. Ma, *Nanoscale* **2019**, 11, 15418–15439.
- [9] Y. Yang, G. Zheng, Y. Cui, *Chem. Soc. Rev.* **2013**, 42, 3018.
- [10] A. Fotouhi, D. Auger, L. O'Neill, T. Cleaver, S. Walus, *Energies* **2017**, 10, 1937.



## FULL PAPER

- [11] W. Cao, J. Zhang, H. Li, *Energy Storage Mater.* **2020**, *26*, 46–55.
- [12] T. Ould Ely, D. Kamzabek, D. Chakraborty, M. F. Doherty, *ACS Appl. Energy Mater.* **2018**, *1*, 1783–1814.
- [13] M. T. McDowell, I. Ryu, S. W. Lee, C. Wang, W. D. Nix, Y. Cui, *Adv. Mater.* **2012**, *24*, 6034–6041.
- [14] D. Lin, Z. Lu, P.-C. Hsu, H. R. Lee, N. Liu, J. Zhao, H. Wang, C. Liu, Y. Cui, *Energy Environ. Sci.* **2015**, *8*, 2371–2376.
- [15] Z. Karkar, D. Mazouzi, C. R. Hernandez, D. Guyomard, L. Roué, B. Lestriez, *Electrochim. Acta* **2016**, *215*, 276–288.
- [16] M. Ashuri, Q. He, L. L. Shaw, *Nanoscale* **2016**, *8*, 74–103.
- [17] C. K. Chan, H. Peng, G. Liu, K. McIlwrath, X. F. Zhang, R. A. Huggins, Y. Cui, *Nat. Nanotechnol.* **2008**, *3*, 31–35.
- [18] N. Liu, H. Wu, M. T. McDowell, Y. Yao, C. Wang, Y. Cui, *Nano Lett.* **2012**, *12*, 3315–3321.
- [19] S. Chae, S.-H. Choi, N. Kim, J. Sung, J. Cho, *Angew. Chemie Int. Ed.* **2020**, *59*, 110–135.
- [20] M. R. Al Hassan, A. Sen, T. Zaman, M. S. Mostari, *Mater. Today Chem.* **2019**, *11*, 225–243.
- [21] X. Zuo, J. Zhu, P. Müller-Buschbaum, Y.-J. Cheng, *Nano Energy* **2017**, *31*, 113–143.
- [22] A. Manthiram, Y. Fu, S.-H. Chung, C. Zu, Y.-S. Su, *Chem. Rev.* **2014**, *114*, 11751–11787.
- [23] R. Cao, W. Xu, D. Lv, J. Xiao, J.-G. Zhang, *Adv. Energy Mater.* **2015**, *5*, 1402273.
- [24] J. Zheng, M. Gu, M. J. Wagner, K. A. Hays, X. Li, P. Zuo, C. Wang, J.-G. Zhang, J. Liu, J. Xiao, *J. Electrochem. Soc.* **2013**, *160*, A1624–A1628.
- [25] U. Zubair, D. Versaci, M. Umer, J. Amici, C. Francia, S. Bodoardo, *Mater. Today Commun.* **2021**, *26*, 101970.
- [26] C. Zhang, H. Bin Wu, C. Yuan, Z. Guo, X. W. (David) Lou, *Angew. Chemie Int. Ed.* **2012**, *51*, 9592–9595.
- [27] P. Gao, S. Xu, Z. Chen, X. Huang, Z. Bao, C. Lao, G. Wu, Y. Mei, *ACS Appl. Mater. Interfaces* **2018**, *10*, 3938–3947.
- [28] R. Kardooni, A. R. Kiasat, N. Eskandari Sabzi, *Res. Chem. Intermed.* **2020**, *46*, 1857–1868.
- [29] L. Wang, B. Chen, Z. Meng, B. Luo, X. Wang, Y. Zhao, *Electrochim. Acta* **2016**, *188*, 135–144.
- [30] S. Qing-feng, W. Xian-ming, W. Xian-wen, W. Zhi-ru, L. Jing-li, *Ionics (Kiel)* **2020**, *26*, 2217–2223.
- [31] R. Chen, J. Lai, Y. Li, M. Cao, S. Chen, F. Wu, *RSC Adv.* **2016**, *6*, 103364–103371.
- [32] J. Ye, C. Li, *Ionics (Kiel)* **2020**, *26*, 2845–2853.
- [33] F. Caldera, M. Tannous, R. Cavalli, M. Zanetti, F. Trotta, *Int. J. Pharm.* **2017**, *531*, 470–479.
- [34] N. Rafati, A. Zarrabi, F. Caldera, F. Trotta, N. Ghias, *J. Microencapsul.* **2019**, *36*, 715–727.
- [35] U. Zubair, A. Anceschi, F. Caldera, M. Alidoost, J. Amici, C. Francia, M. Zanetti, F. Trotta, S. Bodoardo, N. Penazzi, *J. Solid State Electrochem.* **2017**, *21*, 3411–3420.
- [36] G. S. Ghodake, S. K. Shinde, A. A. Kadam, R. G. Saratale, G. D. Saratale, M. Kumar, R. R. Palem, H. A. AL-Shwaiman, A. M. Elgorban, A. Syed, D.-Y. Kim, *J. Clean. Prod.* **2021**, *297*, 126645.
- [37] C. Ceccone, M. Zanetti, A. Anceschi, F. Caldera, F. Trotta, P. Bracco, *Polym. Degrad. Stab.* **2019**, *161*, 277–282.
- [38] M. Zanetti, A. Anceschi, G. Magnacca, G. Spezzati, F. Caldera, G. P. Rosi, F. Trotta, *Microporous Mesoporous Mater.* **2016**, *235*, 178–184.
- [39] D. Wu, Y. Liang, X. Yang, Z. Li, C. Zou, X. Zeng, G. Lv, R. Fu, *Microporous Mesoporous Mater.* **2008**, *116*, 91–94.
- [40] D. Zhou, M. Liu, Q. Yun, X. Wang, Y.-B. He, B. Li, Q.-H. Yang, Q. Cai, F. Kang, *Small* **2017**, *13*, 1602015.
- [41] L. Zhang, C. Zhao, Q. Jian, M. Wu, T. Zhao, *J. Power Sources* **2021**, *506*, 230174.
- [42] R. Mo, Z. Lei, D. Rooney, K. Sun, *Energy Storage Mater.* **2019**, *23*, 284–291.
- [43] A. Krause, S. Dörfler, M. Piwko, F. M. Wissner, T. Jaumann, E. Ahrens, L. Giebler, H. Althues, S. Schädlich, J. Grothe, A. Jeffery, M. Grube, J. Brückner, J. Martin, J. Eckert, S. Kaskel, T. Mikolajick, W. M. Weber, *Sci. Rep.* **2016**, *6*, 27982.
- [44] D. He, X. Huang, M. Li, *Carbon N. Y.* **2019**, *141*, 531–541.
- [45] X. Han, Z. Zhang, H. Chen, R. You, G. Zheng, Q. Zhang, J. Wang, C. Li, S. Chen, Y. Yang, *J. Power Sources* **2019**, *436*, 226794.

## FULL PAPER

- [46] X. Zhu, S. H. Choi, R. Tao, X. Jia, Y. Lu, *J. Alloys Compd.* **2019**, 791, 1105–1113.
- [47] Y. Li, R. Wang, J. Zhang, J. Chen, C. Du, T. Sun, J. Liu, C. Gong, J. Guo, L. Yu, J. Zhang, *Ceram. Int.* **2019**, 45, 16195–16201.
- [48] J. Wang, S. Y. Chew, Z. W. Zhao, S. Ashraf, D. Wexler, J. Chen, S. H. Ng, S. L. Chou, H. K. Liu, *Carbon N. Y.* **2008**, 46, 229–235.
- [49] D.-W. Wang, G. Zhou, F. Li, K.-H. Wu, G. Q. (Max) Lu, H.-M. Cheng, I. R. Gentle, *Phys. Chem. Chem. Phys.* **2012**, 14, 8703.
- [50] X. Yu, J. Xie, J. Yang, H. Huang, K. Wang, Z. Wen, *J. Electroanal. Chem.* **2004**, 573, 121–128.
- [51] Y.-X. Wang, L. Huang, L.-C. Sun, S.-Y. Xie, G.-L. Xu, S.-R. Chen, Y.-F. Xu, J.-T. Li, S.-L. Chou, S.-X. Dou, S.-G. Sun, *J. Mater. Chem.* **2012**, 22, 4744.
- [52] M. Bláha, A. Suchánková, E. Watzlová, J. Prokeš, O. Pop-Georgievski, *Chem. Pap.* **2017**, 71, 329–338.
- [53] G. Li, J. Sun, W. Hou, S. Jiang, Y. Huang, J. Geng, *Nat. Commun.* **2016**, 7, 10601.
- [54] M. Barghamadi, A. S. Best, A. I. Bhatt, A. F. Hollenkamp, P. J. Mahon, M. Musameh, T. Rüther, *Electrochim. Acta* **2015**, 180, 636–644.
- [55] X. Han, J. Cai, X. Wang, Y. Liu, H. Zhou, X. Meng, *Mater. Today Commun.* **2021**, 26, 101934.
- [56] E. Peled, M. Goor, I. Schektman, T. Mukra, Y. Shoval, D. Golodnitsky, *J. Electrochem. Soc.* **2017**, 164, A5001–A5007.
- [57] B. Rossi, S. Caponi, F. Castiglione, S. Corezzi, A. Fontana, M. Giarola, G. Mariotto, A. Mele, C. Petrillo, F. Trotta, G. Viliani, *J. Phys. Chem. B* **2012**, 116, 5323–5327.
- [58] X. GUAN, G. CHEN, C. SHANG, *J. Environ. Sci.* **2007**, 19, 438–443.
- [59] Y. L. Khung, S. H. Ngalim, L. Meda, D. Narducci, *Chem. - A Eur. J.* **2014**, 20, 15151–15158.
- [60] S.-J. Kim, M.-C. Kim, S.-B. Han, G.-H. Lee, H.-S. Choe, S.-H. Moon, D.-H. Kwak, S. Hong, K.-W. Park, *J. Ind. Eng. Chem.* **2017**, 49, 105–111.
- [61] Y. Bie, J. Yang, W. Lu, Z. Lei, Y. Nuli, J. Wang, *Electrochim. Acta* **2016**, 212, 141–146.
- [62] F. Zhang, X. Yang, Y. Xie, N. Yi, Y. Huang, Y. Chen, *Carbon N. Y.* **2015**, 82, 161–167.
- [63] Q. Li, X. Liu, X. Han, Y. Xiang, G. Zhong, J. Wang, B. Zheng, J. Zhou, Y. Yang, *ACS Appl. Mater. Interfaces* **2019**, 11, 14066–14075.
- [64] Y. Jin, N.-J. H. Kneusels, L. E. Marbella, E. Castillo-Martínez, P. C. M. M. Magusin, R. S. Weatherup, E. Jónsson, T. Liu, S. Paul, C. P. Grey, *J. Am. Chem. Soc.* **2018**, 140, 9854–9867.
- [65] T. Jaumann, J. Balach, M. Klose, S. Oswald, U. Langklotz, A. Michaelis, J. Eckert, L. Giebeler, *Phys. Chem. Chem. Phys.* **2015**, 17, 24956–24967.
- [66] T. Jaumann, J. Balach, M. Klose, S. Oswald, J. Eckert, L. Giebeler, *J. Electrochem. Soc.* **2016**, 163, A557–A564.
- [67] V. Etacheri, U. Geiger, Y. Gofer, G. A. Roberts, I. C. Stefan, R. Fasching, D. Aurbach, *Langmuir* **2012**, 28, 6175–6184.
- [68] A. Rezaqita, M. Sauer, A. Foelske, H. Kronberger, A. Trifonova, *Electrochim. Acta* **2017**, 247, 600–609.
- [69] N.-S. Choi, K. H. Yew, K. Y. Lee, M. Sung, H. Kim, S.-S. Kim, *J. Power Sources* **2006**, 161, 1254–1259.
- [70] B. Key, M. Morcrette, J.-M. Tarascon, C. P. Grey, *J. Am. Chem. Soc.* **2011**, 133, 503–512.
- [71] G. M. Carroll, M. C. Schulze, T. R. Martin, G. F. Pach, J. E. Coyle, G. Teeter, N. R. Neale, *ACS Appl. Energy Mater.* **2020**, 3, 10993–11001.
- [72] V. L. Chevrier, L. Liu, D. B. Le, J. Lund, B. Molla, K. Reimer, L. J. Krause, L. D. Jensen, E. Figgemeier, K. W. Eberman, *J. Electrochem. Soc.* **2014**, 161, A783–A791.
- [73] C. C. Nguyen, B. L. Lucht, *J. Electrochem. Soc.* **2014**, 161, A1933–A1938.
- [74] J. Guo, A. Omar, A. Urbanski, S. Oswald, P. Uhlmann, L. Giebeler, *ACS Appl. Energy Mater.* **2019**, 2, 4411–4420.
- [75] K. Ogata, E. Salager, C. J. Kerr, A. E. Fraser, C. Ducati, A. J. Morris, S. Hofmann, C. P. Grey, *Nat. Commun.* **2014**, 5, 3217.
- [76] R. Elazari, G. Salitra, G. Gershinsky, A. Garsuch, A. Panchenko, D. Aurbach, *Electrochem. commun.* **2012**, 14, 21–24.
- [77] X. Pu, G. Yang, C. Yu, *Nano Energy* **2014**, 9, 318–324.
- [78] U. Zubair, J. Amici, S. M. Crespiera, C. Francia, S.

WILEY-VCH

---

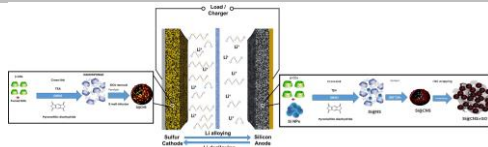


## FULL PAPER

## Entry for the Table of Contents

## FULL PAPER

A facile production strategy to synthesize Si and S directly within porous carbon derived from cyclodextrin nanosponges. These materials act as high capacity electrodes in Lithiated Si-S cells.



M. Alidoost, A. Mangini, F. Caldera, A. Anceschi, J. Amici\*, D. Versaci, L. Fagiolari, F. Trotta, C. Francia, F. Bella, S. Bodoardo

**Page No. – Page No.**  
**Micro-mesoporous carbons from cyclodextrin nanosponges enabling high capacity silicon anodes and sulfur cathodes for lithiated Si-S batteries**